CONTENTS

COVER   The innate immune system is the first line of defense encountered by invading pathogens and plays a fundamental role in the early stages of infection before adaptive immunity becomes effective. Defensins, a family of arginine-rich cationic antimicrobial peptides, are affiliated with the innate immune system and possess broad-spectrum antimicrobial activity against various microorganisms, including bacteria, fungi, viruses, and even protozoa. As birds are important sources and reservoirs of zoonotic infections that cause local outbreaks of infection in human populations, to reveal the immunological roles of defensin genes and the underlying mechanisms become critical. However, despite many previous attempts, only limited information is available regarding the organization and evolution of defensing genes. In this study, the analysis of the genomic structure and evolution of beta-defensin genes in the golden pheasant of Galliformes and hwamei of Passeriformes reveal that birds are able to duplicate defensin genes and express more gene copies in the respiratory system to achieve greater immune defense. These results will help to further understand the evolution and immunological roles of defensin genes and provide a potential basis for the disease resistance studies in the future (see the article by Hui Chen et al. on page 679).
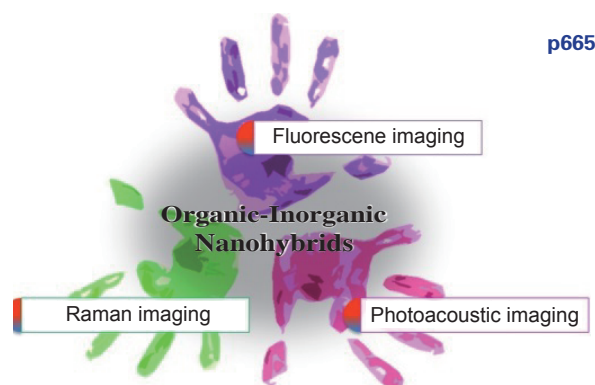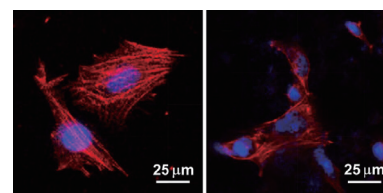
Volume 60   Number 7
April   2015

PROGRESS

p665

REVIEW

Organic-Inorganic Nanohybrids

Fluorescene imaging

Raman imaging

Photoacoustic imaging

p691

ARTICLES

25 μm   25 μm

p726

Article · Engineering Sciences

Microfabricated ultra-thin all-polymer thermal ground planes

Ryan Lewis · Li-Anne Liew · Shanshan Xu ·
Yung-Cheng Lee · Ronggui Yang
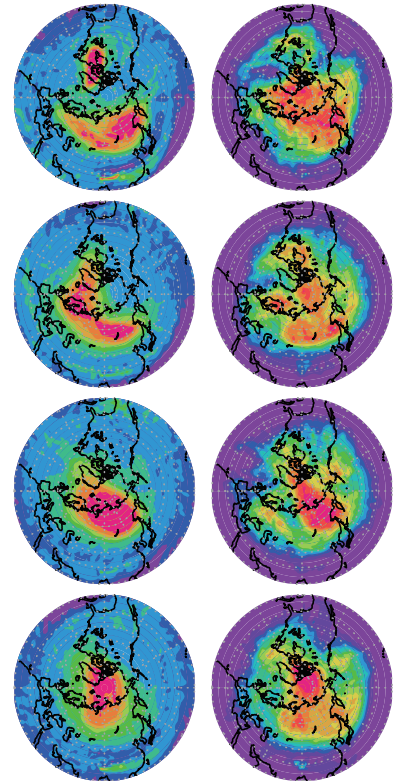
Abstract Thermal ground planes, or planar heat pipes, can provide highly effective heat transfer by utilizing phase change of an encapsulated fluid. In this article, a flexible thermal ground plane (FTGP) was fabricated using polymer materials. Kapton was employed as a casing material while micropatterned SU-8 was used to provide both a liquid wicking structure and pillars to support the casing over a vapor core. An ultra-thin TiO_2 film was deposited over the SU-8 and Kapton via atomic layer deposition, which acted as both a moisture barrier and a hydrophilic coating on polymer surfaces. The assembled FTGP has a thickness of 0.30 mm, an active area of 20 mm × 60 mm, heater area of 20 mm × 10 mm, and can operate with a heat load up to 9.54 W, with an effective thermal conductivity up to 541 W/(m K).

Keywords Flexible electronics · Heat pipe · Electronics cooling · Thermal ground plane

1 Introduction

Micro heat pipes have been developed over the past two decades for thermal management of electronic devices [1–3]. Two-dimensional thermal ground planes (TGPs) or flat heat pipes have recently attracted great interests for mobile electronics. In such devices, heat enters a wicked evaporator section through the casing material, and the liquid permeating the wick absorbs the heat and evaporates. The vapor flows from the evaporator through an adiabatic section to the condenser, where it rejects the heat as it condenses. The condensate permeates the wicking structure and is pulled back to the evaporator by capillary pressure, completing the closed-loop thermodynamics cycle. Many previous TGPs have been fabricated by metal or ceramic microprocessing [4–6], but these prove challenging for flexible electronics applications.

Various polymer flexible thermal ground planes (FTGPs) have been developed, which use aluminized Mylar as the casing material and woven copper mesh bonded to electroplated copper micropillars as the wicking structure [7, 8], as well as silicone rubber as the casing material and multi-layer copper mesh as the wick [9]. All-polymer FGTPs are of great interests for wearable electronics and mobile computing, with potential enhancements in weight, flexibility, and manufacturability. An all-polymer FTGP based on extruded polypropylene was developed by McDaniels and Peterson [10], although the thermal performance of the device was not reported. Using commercial woven polymer mesh as the wicking structure, an all-polymer FTGP was developed by Oshman and reported in Ref. [11]. The FTGP was 1.1 mm in thickness. However, the reduction in thickness proved challenging due to the use of the commercial mesh structure. If the wicking structures in all-polymer FTGPs are defined by lithography, we can potentially optimize the device geometries with minimal overall thickness, as that have been done for ultra-thin TGPs made of metal and silicon substrates [5, 6]. Additionally, lithography enables a spatial gradient in the size of channels in the wick, which can potentially further optimize the device performance.

This article demonstrates the design, microfabrication, and testing of an ultra-thin, all-polymer FTGP. The design

R. Lewis (✉) · L.-A. Liew · S. Xu · Y.-C. Lee · R. Yang (✉)
Department of Mechanical Engineering, University of Colorado, Boulder, CO 80309-0427, USA
e-mail: Ryan.J.Lewis-1@Colorado.Edu

R. Yang
e-mail: Ronggui.Yang@Colorado.Edu

considers the size of liquid and vapor flow channels that maximize the difference between capillary pumping pressure and viscous pressure drop due to flow friction. Microfabrication is based on SU-8 patterning to define an array of micropillars as a liquid wicking structure. Additionally, posts of SU-8 are used to support the cladding material and keep it from collapsing when the system is under vacuum. An ultra-thin coating of TiO_2 deposited by atomic layer deposition (ALD) is used as both as an impermeable moisture barrier and to render the surface hydrophilic. The assembled FTGP has an active area of 2 cm × 6 cm and a thickness of 0.3 mm. When tested with an evaporator measuring 2 cm × 1 cm and a condenser measuring 2 cm × 2.5 cm, the maximum heat load is 9.54 W with an effective thermal conductivity up to 541 W/(m K).

2 Experimental methods

2.1 Design

Figure 1a shows the cross-sectional schematics of the FTGP. The wicking structure of the FTGP is composed of an array of micropillars, as shown in Fig. 1b. Liquid flows through the channels between the micropillars, and such spacing provides the small radius necessary for high capillary pumping pressure. Vapor flows through a cavity between the wick and the vapor-side cladding; the height of this vapor core is defined by microposts. Additionally, a

(a)

Vapor cladding 50 μm
Vapor wick 10 μm
Vapor posts 140 μm
Liquid wick 50 μm
Liquid cladding 50 μm

(b)

2.0 cm

Evaporator 1.0 cm — 50 μm × 50 μm pillars 30 μm spacing

0.5 cm — 100 μm × 100 μm pillars 50 μm spacing

Adiabatic (2.5 cm)

3.0 cm — 150 μm × 150 μm pillars

Condenser (2.5 cm)

50 μm
100 μm

0.5 cm

1.0 cm

(c)

Fig. 1 (Color online) **a** Cross-sectional schematics of FTGP, and **b** top-view schematic of the micropillar wick, **c** photograph of the complete FTGP

thin wick above the vapor posts prevents the accumulation of water along the vapor-side cladding. The posts are asterisk-shaped, creating channels for such accumulated water to return to the liquid wick. The design goals for this TGP is to achieve power dissipation of 5 W on an evaporator 1 cm × 2 cm in size with a total thickness of 300 μm over a TGP active area of 2 cm × 6 cm.

Careful consideration must go into the design of the FTGP microstructures in both liquid wicking structure and vapor core. Of particular concern is to ensure that the pressure drop due to viscosity is smaller than the capillary pumping pressure provided by the wicking structure so that the device will not operate under the capillary limit.

The pressure drop through the liquid channels can be calculated for laminar flow according to [12]

$$\Delta P_l = \left(\frac{1}{6}L_e + L_a + \frac{1}{6}L_c\right)\frac{\left(\frac{fRe}{2}\right)\mu_l}{w_{T,l}\delta_l r_h^2}\frac{\dot{Q}}{\Delta h_{fg}\rho_l}. \tag{1}$$

Here, L refers to the length, with the subscripts e, a, and c referring to the evaporator, adiabatic section, and condenser; fRe is the product of the friction factor and Reynolds number, which is a constant that depends on geometry for laminar flow; μ is the viscosity, w_T is the total flow width available to the liquid flow (TGP width less width of SU-8 pillars), δ the height of the flow channel, r_h the hydraulic radius of the flow channel, $\dot{Q}$ the power dissipated, Δh_{fg} the enthalpy change of vaporization, and ρ the density. The subscript l refers to liquid-phase-specific quantities. The hydraulic radius of the flow channel is a function of the channel width (w_c) and height, as $r_h = \delta_l w_c/(\delta_l + w_c)$.

In macro-scale heat pipes or TGPs, the pressure drop associated with vapor flow is often neglected; however, in ultra-thin TGPs, the friction resistance of vapor flow can be dominant. For parallel-plate flow, the hydraulic radius will be equivalent to the vapor core thickness; therefore, the pressure drop of the vapor will be given by

$$\Delta P_v = \left(\frac{1}{6}L_e + L_a + \frac{1}{6}L_c\right)\frac{\left(\frac{fRe}{2}\right)\mu_v}{w_{T,v}\delta_v^3}\frac{\dot{Q}}{\Delta h_{fg}\rho_v}. \tag{2}$$

The capillary pumping pressure is given by the Young–Laplace law for a fluid with surface tension (σ) and capillary radius; for channels between micropillars, the capillary radius will be given by half the channel width:

$$\Delta P_{cap} = 2\sigma/w_c. \tag{3}$$

The sum of the pressure losses due to viscosity dissipation must be less than the capillary pressure. Note that the capillary pressure is independent of the heat load when thermophysical properties are assumed to be constant, while the viscous pressure drops have a linear relationship with heat load. Figure 2a plots the region of successful design in the parameter space for vapor core
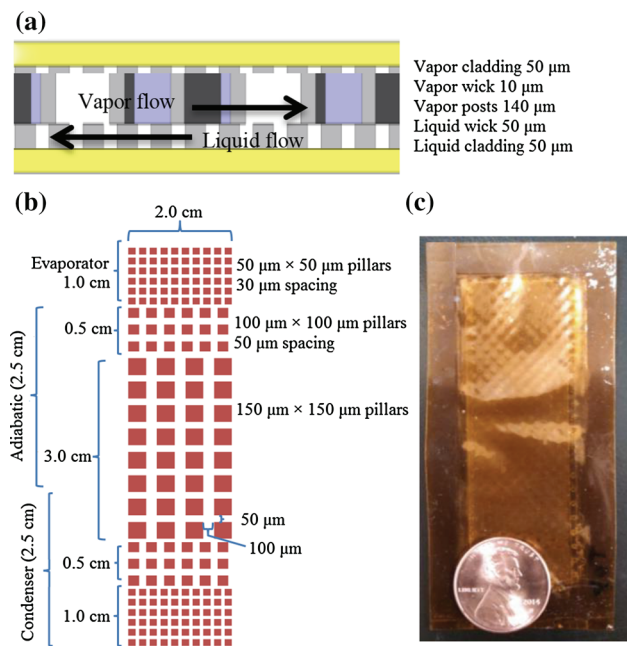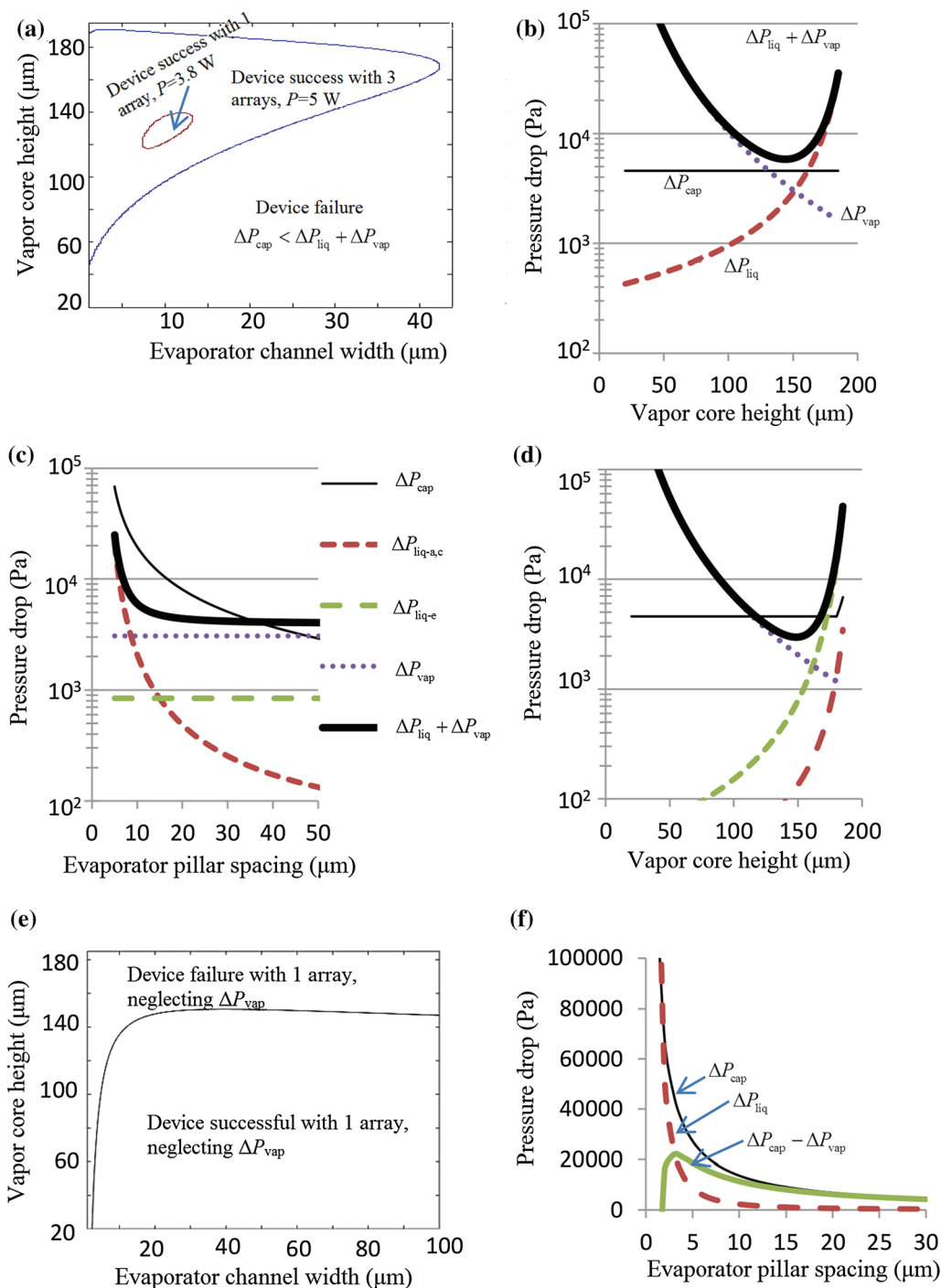
Fig. 2 (Color online) Design of FTGP wicking structure. **a** Boundary of successful design in the parameter space for vapor core height and channel width for a single array of micropillars and a triple array of micropillars. **b** Pressure drop curves for a wick with a single array of micropillars, showing that the capillary pressure is always less than the viscous losses at 5 W power, **c** Pressure drop curve as a function of evaporator/condenser pillar spacing, calculated at a vapor core thickness of 150 µm. **d** Pressure drop curve as a function of vapor core thickness, calculated at a of evaporator/condenser pillar spacing of 30 µm showing a minimum at 150 µm. **e** For reference, a design under the assumption that the vapor pressure drop may be neglected is considered, with a boundary of successful design. **f** Liquid pressure drop and capillary curve with neglected vapor pressure drop at a liquid thickness of 180 µm, showing a maximum pressure difference at a spacing of 3.5 µm

height and channel width for a single array of micropillars. For these calculations, thermophysical properties of saturated water at 45 °C are used; evaporator, condenser,

and adiabatic lengths were as defined in Fig. 1b; liquid and vapor heights were constrained such that the total height is 200 µm; $w_{T,l}$ was 32 % of the 2 cm active TGP width,

giving 6.5 mm; and $w_{T,v}$ was 80 % of the active width, at 16 mm. Such calculation shows that there is no combination of pillar spacing and vapor core height that will ensure capillary pumping pressure overpowers the viscous losses at the design goal of 5 W, as shown in Fig. 2b. The highest power dissipation that can be sustained is 3.8 W, with a vapor height of 125 μm and a channel width in the range 9–15 μm, as shown in Fig. 2a.

Therefore, a second wick design is considered in which three arrays are used. In the evaporator and condenser sections, an array with smaller pillars and smaller spacing provides a higher capillary force. In the adiabatic section, an array with a wide spacing between pillars allows liquid to flow with low viscous loss; additionally, there is a transitional section between wide and narrow arrays. The design is shown in Fig. 1b.

To lower the pressure drop due to liquid friction, the adiabatic-section liquid channels should be as large as possible in the direction of the flow, but they must also be small enough to provide a capillary force that overcomes a gravitation pressure drop. This occurs at a maximum width of 100 μm. Perpendicular to the flow, channels need half the spacing due to the non-confined nature of rising liquid. The evaporator/condenser spacing is chosen at 30 μm as an upper bound (allowing for SU-8 overdevelopment), as in Fig. 2c. The vapor core thickness is optimized at 150 μm to provide the lowest overall pressure drop, in Fig. 2d; this thickness will be divided into the vapor posts and vapor wick.

For reference, Fig. 2e and f, consider the design of a TGP in which pressure drop from the vapor flow may be neglected. If vapor core effects can be neglected, a TGP can be successful with a single wick array at 5 W, provided that the vapor core is <140 μm (i.e., the wicking structure is >60 μm), and spacing between the pillars is >2 μm. According to Fig. 2f, the maximum excess capillary pressure occurs at a pillar spacing of 3.5 μm. Clearly, this is a very different design optimum compared with the design in Fig. 2c–d, in which the vapor pressure drop is accounted for.

2.2 Fabrication and assembly

Figure 3a shows the SU-8 micropillars developed for our wick design. Following standard SU-8 processing techniques, a 50-μm-thick SU-8 3050 layer is spin-coated onto 50-μm-thick Kapton film at 3000 r/min, pre-baked at 95 °C for 15 min, exposed to 400 mJ/cm^2 of 340 nm UV radiation, post-baked at 95 °C for 10 min, and developed in SU-8 developer. The SU-8 and Kapton form the liquid cladding and wicking layers of the FTGP.

An issue with polymer-based FTGPs is that of condensate collecting on the vapor-side cladding layer and causing a blockage in the vapor channel. To ameliorate such an issue, a small wicking layer of SU-8 is deposited on the
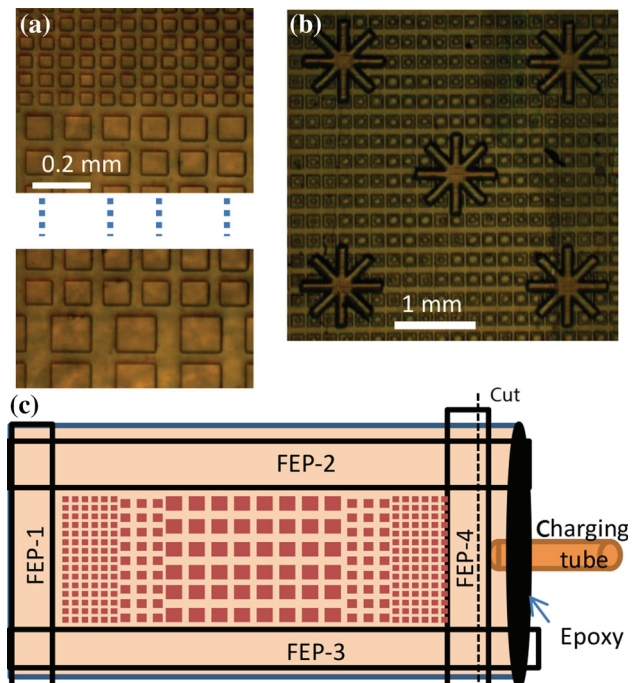

Fig. 3 (Color online) Micrograph images of: **a** micropillar arrays of both the narrow pillars for the evaporator/condenser, the large pillars for the adiabatic region, and the transitional array, **b** vapor core posts and vapor wick pillar array. **c** Schematic of TGP assembly

vapor-side Kapton layer as well. This vapor wick is 10 μm thick, composed of SU-8 10, and uses the same photomask as the liquid wick. After spinning (3000 r/min), pre-baking (95 °C, 5 min), irradiating (250 mJ/cm^2), and post-baking the "vapor wick" layer, a thicker layer of SU-8 3050 is deposited in order to provide the vapor channel pillars. The 150 μm layer is deposited by spin-coating and soft-baking 2×70 μm SU-8 3050 layers, each spun at 1600 r/min. The first layer is pre-baked at 95 °C for 30 min before applying the second layer. The two layers are then pre-baked together at 95 °C for 90 min, before irradiating with 500 mJ/cm^2, and post-baking at 95 °C for 30 min. Finally, both the vapor wick and posts are developed simultaneously in SU-8 developer. The resulting structural layer is shown in Fig. 3b.

The two Kapton and SU-8 structural layers are then coated with ALD films to provide hydrophilic surface with a moisture barrier. ALD takes place in a commercial reactor in a 1 mbar nitrogen environment at 150 °C. First, a 5 nm Al_2O_3 film is grown as an adhesion layer via 50 cycles of trimethylaluminum and water; second, a 20 nm film of TiO_2 is grown as a hydrophilic and barrier layer via 250 cycles of titanium(iv)tetrachloride and water. It has been shown previously that ALD TiO_2 provides a superior barrier in aqueous environments, when used in conjunction with an ALD Al_2O_3 nucleation layer [13].

The ALD-coated polymer layers are sealed together using FEP, thermo-pressed along the three sides of the perimeter, labeled FEP-1, FEP-2, and FEP-3 in Fig. 3c. Thermo-pressing occurs at 300 °C and 75 psi (1 kPa = 0.145 psi) for 20 s. The final side is epoxy bonded to a copper tube to allow evacuation and charging of 0.15 mL water, as in Ref. [8]. The optimal water charge of 0.15 mL is determined experimentally. After water-charging, a final FEP bond (FEP-4 in Fig. 3c) isolates the TGP from the copper tube and it can be cut away. The final mass of the FTGP is 0.85 g, a factor of 4 lower than an equally sized copper heat spreader.

2.3 Testing

The test apparatus is shown in schematically in Fig. 4a and is adapted from previous work [8]. Heat is supplied to the evaporator of the FTGP by a small ceramic heater; heat is removed from the condenser by an aluminum block with a known 1 cm × 1 cm cross section and linear array of thermocouples down the length. Heat flow out of the FTGP can then be calculated by Fourier's Law. The thermal resistance of the FTGP is given by the ratio of the temperature difference between the evaporator and condenser, with the heat flow through the TGP:

$$R = \Delta T / Q. \tag{4}$$

In Eq. (4), the heat flow through the condenser block is used as Q, rather than the input electrical power to the ceramic heater. Due to parasitic heat losses associated with the heater, only 73 % of the Joule heating goes into the FTGP; the other 27 % will escape through the leads or mounting bracket, for example [8].

Figure 4c shows the evaporator and condenser temperatures as a function of power. The test was discontinued after 9.5 W of power as the evaporator temperature approached the 100 °C. Operation above this temperature would result in a positive pressure difference across the FTGP which would damage the FEP seal. The average temperature at 9.5 W was 61 °C; using the thermophysical properties of saturated water at 61 °C and our FTGP's geometry, Eqs. (1)–(3) predict that the viscous pressure drops will overcome the capillary pressure at 11.35 W. However, we are not able to evaluate whether that is the limit of the FTGP's performance due to the high evaporator temperature.
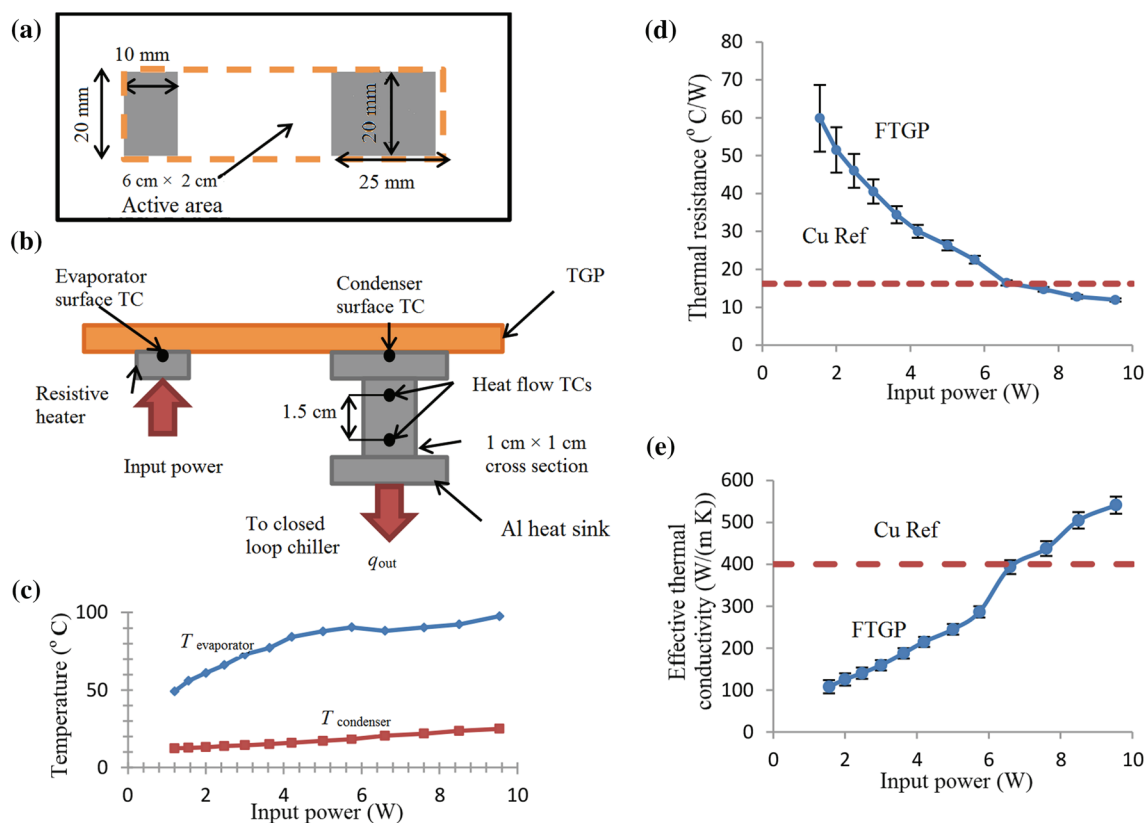

Fig. 4 (Color online) **a** Top-view and **b** side-view schematic of test setup to measure thermal resistance of the FTGP, adapted from Ref. [8]. **c** Evaporator and condenser temperatures measured as a function of input power, **d** measured thermal resistance of FTGP (dots/solid line) and copper (dashed line), and **e** corresponding effective thermal conductivity

The thermal resistance is measured as a function of various input powers (electrical power applied to the heater), as shown in Fig. 4d. Additionally, a reference copper heat spreader measuring 20 mm $\times$ 60 mm $\times$ 0.30 mm was tested in the same test setup, and its resistance is also shown in Fig. 4d, giving a constant value of 16.2 °C/W. Figure 4e gives the effective thermal conductivity of the FTGP, given by the ratio of copper and FTGP thermal resistance, multiplied by copper's thermal conductivity: $k_{FTGP} = k_{Cu}(R_{Cu}/R_{FTGP})$. Error bars in Fig. 4d and e are the result of instrumentation precision limits associated with the test setup.

Note that the effective thermal conductivity increases with increasing power. Increasing the power increases the temperature of the saturated vapor, resulting in a higher vapor saturation density and more effective vapor thermal transport. For input powers greater than 7.6 W, the vapor temperature is high enough that the FTGP has an effective thermal conductivity above copper.

The lowest resistance occurs at 9.54 W with a value of 11.92 °C/W, which is 73.1 % that of the reference copper, giving the FTGP an effective thermal conductivity of 541 W/(m K). This is three orders of magnitude higher than the constituent polymer materials, in the range of (0.1–1) W/(m K), from which the FTGP is fabricated.

3 Conclusion

A flexible thermal ground plane was fabricated using polyimide films as cladding material and lithography-defined SU-8 micropillars as the wicking structure, with a total thickness of 0.3 mm. To achieve such thickness, the vapor core thickness and pillar spacing were optimized to minimize the overall pressure drop in the FTGP. The polymer structures were coated with ALD TiO_2 to provide a hydrophilic and hermetic coating. With 0.15 mL water, the 2 cm $\times$ 6 cm $\times$ 0.3 mm TGP measured a resistance as low as 11.92 °C/W, giving it an effective thermal conductivity of 541 W/(m K).

References

1. Peterson GP (1994) An introduction to heat pipes. Wiley, New York
2. Gillot C, Laï A, Ivanova M et al (2004) Experimental study of a flat silicon heat pipe with microcapillary grooves. In: InterSociety conference on thermal and thermomechanical phenomena in electronic systems, IEEE. XXIX-748
3. Oshman C, Shi BCL, Yang RG et al (2011) The development of polymer-based flat heat pipes. J Microelectromech Syst 20:410–417
4. Ju YS, Kaviany M, Nam Y et al (2013) Planar vapor chamber with hybrid evaporator wicks for the thermal management of high-heat-flux and high-power optoelectronic devices. Int J Heat Mass Transfer 60:163–169
5. Ding C, Soni G, Bozorgi P et al (2010) A flat heat pipe architecture based on nanostructured titania. J Microelectromech Syst 19:878–884
6. Cai Q, Chen BC, Tsai C et al (2010) Development of scalable silicon heat spreader for high power electronic devices. J Therm Sci Eng Appl 1:041009
7. Oshman C, Li Q, Liew LA et al (2013) Flat flexible polymer heat pipes. J Micromech Microeng 23:015001
8. Oshman C, Li Q, Liew LA et al (2012) Thermal performance of a flat polymer heat pipe heat spreader under high acceleration. J Micromech Microeng 22:045018
9. Hsieh SS, Yang YR (2013) Design, fabrication and performance tests for a polymer-based flexible flat heat pipe. Energy Conv Manag 70:10–19
10. McDaniels D, Peterson GP (2001) Investigation of polymer based micro heat pipes for a flexible spacecraft radiator. ASME Publ HTD 369:423–434
11. Bar-Cohen A, Matin K, Jankowski N et al (2015) Two-phase thermal ground planes: technology development and parametric results. J Electron Packag 137:010801
12. Faghri A (1995) Heat pipe science and technology. Taylor and Francis, Washington
13. Abdulagatov AI, Yan Y, Cooper JR et al (2011) Al_2O_3 and TiO_2 atomic layer deposition on copper for water corrosion resistance. ACS Appl Mater Interfaces 3:4593–4601